Coupling of the microphysical and optical properties of an Arctic nimbostratus cloud during the ASTAR 2004 experiment: Implications for light-scattering modeling

Olivier Jourdan, Guillaume Mioche, Timothy J Garrett, Alfons Schwarzenboeck, Jérôme Vidot, Yu Xie, Valery Shcherbakov, Ping Yang, Jean-François Gayet

Coupling of the microphysical and optical properties of an Arctic nimbostratus cloud during the ASTAR 2004 experiment: Implications for light-scattering modeling

Olivier Jourdan,[1] Guillaume Mioche,[1] Timothy J. Garrett,[2] Alfons Schwarzenböck,[1] Jérôme Vidot,[1] Yu Xie,[3] Valery Shcherbakov,[1,4] Ping Yang,[3] and Jean-François Gayet[1]

Received 5 February 2010; revised 28 September 2010; accepted 5 October 2010; published 4 December 2010.

[1] Airborne measurements in an Arctic mixed-phase nimbostratus cloud were conducted in Spitsbergen on 21 May 2004 during the international Arctic Study of Tropospheric Aerosol, Clouds and Radiation (ASTAR) campaign. The in situ instrument suite aboard the Alfred Wegener Institute Polar 2 aircraft included a polar nephelometer (PN), a cloud particle imager (CPI), a Nevzorov probe, and a standard PMS 2DC probe to measure the cloud particle single-scattering properties (at a wavelength of 0.8 μm), and the particle morphology and size, as well as the in-cloud partitioning of ice/water content. The main objective of this work is to present a technique based on principal component analysis and light-scattering modeling to link the microphysical properties of cloud particles to their optical characteristics. The technique is applied to the data collected during the 21 May case study where a wide variety of ice crystal shapes and liquid water fractions were observed at temperatures ranging from −1°C to −12°C. CPI measurements highlight the presence of large supercooled water droplets with diameters close to 500 μm. Although the majority of ice particles were found to have irregular shapes, columns and needles were the prevailing regular habits between −3°C and −6°C while stellars and plates were observed at temperatures below −8°C. The implementation of the principal component analysis of the PN scattering phase function measurements revealed representative optical patterns that were consistent with the particle habit classification derived from the CPI. This indicates that the synergy between the CPI and the PN can be exploited to link the microphysical and shape properties of cloud particles to their single-scattering characteristics. Using light-scattering modeling, we have established equivalent microphysical models based on a limited set of free parameters (roughness, mixture of idealized particle habits, and aspect ratio of ice crystals) that reproduce the main optical features assessed for cloud regions with different particle geometries and liquid water fractions. However, the retrieved bulk microphysical parameters can substantially differ from the measurements (by several times for the effective size and up to 3 orders of magnitude for the number concentration). Several possible explanations for these discrepancies are discussed. The retrievals show that the optical contribution of small particles with sizes lower than 50 μm (droplets and ice crystals) is significant, always exceeding 50% of the total scattering signal, and thus needs to be more accurately quantified. The shattering of large ice crystals on the shrouded inlet of the PN could also strongly affect the retrieved microphysical parameters.

Citation: Jourdan, O., G. Mioche, T. J. Garrett, A. Schwarzenböck, J. Vidot, Y. Xie, V. Shcherbakov, P. Yang, and J.-F. Gayet (2010), Coupling of the microphysical and optical properties of an Arctic nimbostratus cloud during the ASTAR 2004 experiment: Implications for light-scattering modeling, *J. Geophys. Res.*, *115*, D23206, doi:10.1029/2010JD014016.

[1]Laboratoire de Météorologie Physique, Université Blaise Pascal, OPGC/CNRS UMR 6016, Clermont-Ferrand, France.

[2]Department of Atmospheric Sciences, University of Utah, Salt Lake City, Utah, USA.

[3]Department of Atmospheric Sciences, Texas A&M University, College Station, Texas, USA.

[4]Laboratoire de Météorologie Physique, Institut Universitaire de Technologie de Montluçon, Montluçon, France.

0148-0227/10/2010JD014016

1. Introduction

[2] Climate models indicate that the surface air temperature increase in the arctic will be substantially more pronounced than the average warming of the planet [*Arctic Climate Impact Assessment*, 2004]. Arctic surface conditions strongly complicate cloud radiation feedback processes identified as key uncertainties for the prediction of Arctic and global climate [*Intergovernmental Panel on Climate Change* (*IPCC*), 2001, 2007; *Vavrus*, 2004]. The assessment of the radiative effect of Arctic cloud is hindered by inadequate knowledge of their thermodynamic phase and their geometrical (height, thickness, fractional coverage), microphysical (liquid water fraction, particle size and shape) and optical (cloud optical depth, phase function and single-scattering albedo) properties [see, e.g., *Verlinde et al.*, 2007; *McFarquhar et al.*, 2007]. Remote sensing observations from space performed by active instruments such as CALIOP [*Winker and Trepte*, 2007] and CloudSat [*Stephens et al.*, 2002] of the A-Train constellation could help bridge these gaps and provide detailed characterization of Arctic cloud properties with adequate spatial and temporal coverage. However, since Arctic clouds have a wide variety of physical characteristics [*McFarquhar et al.*, 2007; *Garrett et al.*, 2001; *Gayet et al.*, 2009a, 2009b], detailed optical and microphysical in situ measurements are needed to evaluate satellite products and to develop more appropriate retrieval algorithms, in particular, for glaciated and mixed-phase clouds [*Labonnote et al.*, 2000]. Accurate modeling of mixed-phase cloud single-scattering parameters is the primary condition for interpretation of remote-sensing measurements. In this respect, parameterizations of the scattering and geometric properties for various ice crystal shapes and sizes were developed for shortwave bands [see, e.g., *Yang et al.*, 2000]. Despite substantial progress in this research area, measurements of the optical characteristics of ice crystals in natural conditions are still needed for validation of numerical techniques and for the determination of free parameters of light-scattering models.

[3] The Arctic Study of Tropospheric Aerosol, Clouds and Radiation (ASTAR) 2004 project [*Engvall et al.*, 2008] focused on the detailed in situ characterization of the microphysical and optical properties of Arctic mixed-phase clouds. A unique combination of instruments was installed onboard the Polar 2 aircraft operated by the Alfred Wegener Institute for Polar and Marine Research (AWI). The instruments include a polar nephelometer [*Gayet et al.*, 1997], a cloud particle imager (CPI) [*Lawson et al.*, 2001] and standard 2D-C and Nevzorov probes [*Korolev et al.*, 1998] to measure cloud particle properties in terms of scattering, morphology and size, and in-cloud partitioning of ice/water content. Remote sensing measurements were obtained onboard the Polar 2 aircraft from the Airborne Mobile Aerosol Lidar (AMALi) [*Stachlewska et al.*, 2004].

[4] This paper starts with an overview of the microphysical and optical properties of a mixed-phase nimbostratus cloud observed on 21 May 2004. The cloud case study is characterized by a wide variety of ice crystal shapes and liquid water fractions. An assessment of the relationships between the ice crystal shape and their scattering properties is presented. The methodology consists of implementing a principal component analysis of the polar nephelometer measurements in order to establish a set of representative optical properties correlated to different particle shapes observed in the CPI data. Finally, light-scattering modeling is used to establish equivalent microphysical models based on a limited set of free parameters (roughness, mixture of simple particle habits, aspect ratio) corresponding to the main optical features of the cloud system.

2. Instrumentation, Flight Procedure, and Cloud Situation

2.1. Instrumentation

[5] The experimental campaign ASTAR (Arctic Study on Tropospheric Aerosol and Radiation) was carried out between 15 May and 19 June 2004, by operating a specially equipped Dornier 228-101 aircraft (Polar 2) owned by the Alfred Wegener Institute of Polar and Marine Research (AWI). The instruments used for the determination of the microphysical and optical properties of Arctic clouds included four independent techniques: the polar nephelometer (PN), the cloud particle imager (CPI), the PMS 2D-C probe, and the Nevzorov probe. The combination of these techniques provides a description of cloud particles within a size range varying from a few micrometers (typically 3 μm for the PN) to about two millimeters (for the CPI probe). The method of data processing, the reliability of the instruments and the uncertainties of the derived microphysical and optical parameters were described in detail by *Gayet et al.* [2006, 2009a].

[6] The polar nephelometer [*Gayet et al.*, 1997] measures the angular scattering pattern (nonnormalized scattering phase function) of an ensemble of cloud particles (i.e., water droplets, ice crystals or a mixture of these particles) ranging from a few micrometers to approximately 1 mm in diameter. The measurements are performed at a wavelength of 0.8 μm with scattering angles ranging from ±15° to ±162° and with a resolution of 3.5°. In general, 32 scattering angles are available. Measurements at nearly forward and backward directions ($\theta < 15°$ and $\theta > 162°$) are not reliable due to the diffracted light pollution caused by the edges of holes drilled on the paraboloidal mirror. The instrument provides a continuous sampling volume by integrating the measured signals of each detector over a period selected by the operator (typically 100 ms). The average errors of the angular scattering coefficients (ASC) measurements lie between 3% to 5% for scattering angles ranging from 15° to 162° (with a maximum error of 20% at 162°) [*Shcherbakov et al.*, 2006]. Direct measurement of the scattering phase function allows particle type (water droplets or ice crystals) to be distinguished and calculation of the optical parameters to be performed, i.e., the extinction coefficient and asymmetry parameter. Comparisons between PMS-FSSP-100 and polar nephelometer (PN) measurements in stratocumulus clouds showed that the uncertainty of the extinction coefficient (s_{ext}) is 25% [*Gayet et al.*, 2002a]. In this paper, the asymmetry parameter (g) is assessed based on the ASC measurements documented between 15° and 155°. We follow the methodology proposed by *Gerber et al.* [2000] assuming that the fraction of energy f scattered into angles smaller than 15° is constant and equal to 0.56, regardless of the cloud composition. The absolute error on the asymmetry parameter is expected to range approximately between ±0.04 [*Gerber*

et al., 2000; *Garrett et al.*, 2001; *Gayet et al.*, 2002a] and ±0.05 (for clouds dominated by large ice crystals).

[7] The CPI registers cloud-particle images on a solid state, one million pixel digital charge-coupled device (CCD) camera by freezing the motion of the particle using a 40 ns pulsed, high-power laser diode [*Lawson et al.*, 2001]. Each pixel in the CCD camera array has an equivalent size in the sample area of 2.3 μm. In the present study, the CPI's region of interest (ROI) minimum size is set up to 10 pixels. Therefore particles with sizes ranging approximately from 25 μm to 2 mm are imaged. The method of data and image processing as well as the calibration of the CPI are described in detail by *Gayet et al.* [2009a]. Accordingly, a 5 s running average is applied during the data processing in order to improve the statistical significance of low particle concentrations. Additionally, *Gayet et al.* [2009b] showed that CPI and PMS 2D-C measurements performed in different mixed-phase clouds conditions were in good agreement. Therefore, the CPI errors on the size distributions and derived microphysical parameters are expected to be of the same order of those obtained with the PMS 2D-C instrument: up to 75% on the particle concentration and 100% on the ice water content (IWC) [*Gayet et al.*, 2002b].

[8] The PMS 2D-C instrument was also installed on the Polar 2 aircraft. Due to some intermittent failures which occurred on the data acquisition system, the available data are not discussed in this study but have been used (when reliable) in intercomparisons with the CPI measurements [see *Gayet et al.*, 2009a, Appendix A]. The PMS 2D-C probe provides information on particle size and shape for the size range 25–800 μm.

[9] The shallow cone Nevzorov liquid water content (LWC) and total water content (TWC) instrument is a constant-temperature hot-wire probe designed for aircraft measurements of the liquid and ice water content of clouds [*Korolev et al.*, 1998]; the uncertainties on these quantities have originally been evaluated to 15% and 20%, respectively [*Korolev et al.*, 1998, 2003]. However, more recently, *Korolev et al.* [2008] showed that the shallow cone Nevzorov probe underestimates the IWC by a factor of 3 compared to a more reliable version of the probe with a cone with a sharper angle (deep cone Nevzorov instrument). Consequently, the IWC and TWC data derived from this instrument were not used in this paper. Additionally, the accuracy on LWC measurements could also be affected (underestimated) when large droplets (drizzle) are sampled [*Schwarzenboeck et al.*, 2009].

[10] It also should be pointed out that the accuracies of microphysical measurements could seriously be hampered by the shattering of large ice crystals on probes with shrouded inlets (PN and CPI for instance) [*Korolev and Isaac*, 2005; *Heymsfield*, 2007]. For particle diameters larger than about 100 μm, the number of shattered particles increases with the concentration of large particles.

2.2. Meteorological Situation and Flight Procedure

[11] The observations discussed in this paper were obtained during the Polar 2 flight on 21 May 2004 (between 0930 and 1130 UTC) in the southeast of the Svalbard Archipelago across the Storfjorden. Figure 1 represents the MODIS satellite image at 1010 UTC and gives an overview of the cloud situation. The weather situation over the observation area was characterized by a warm front created by a low-pressure system south of Svalbard, leading to the formation of a deep nimbostratus cloud system. The Polar 2 flight consisted of two main cloud vertical soundings from about 100 m/−1°C (the lowest possible altitude above the sea level) to 3000 m/−12°C (aircraft ceiling). These soundings included in-cloud sequences at several constant levels (2500 m, 1950 m, 1450 m, 950 m, 500 m and 150 m for the descending profile and 1450 m, 1950 m, 2450 m and 2950 m for the ascending profile). Each sequence lasted about 10 min (or 50 km long) with a U-turn maneuver at the end of the sequence. The descending profile was carried out from 0930 to 1040 UTC and the climbing profile from 1040 to 1130 UTC.

2.3. In Situ Measurements: Overview of the Cloud System Microphysical and Optical Properties

[12] The purpose of this section is to give a brief overview of the microphysical and optical properties of the cloud system. Figures 2a–2d represent the average vertical profiles of cloud parameters obtained during the descending track of the aircraft while Figures 2e–2h correspond to the ascending track. The cloud parameters are: the number concentration and the mean diameter of particles larger than 100 μm measured by the CPI (Figures 2a and 2e); the liquid water content and the ice water content deduced from the Nevzorov probe and the CPI, respectively (Figures 2b and 2f); the asymmetry factor and the extinction coefficient derived from the polar nephelometer (Figures 2c and 2g); and, the air temperature and the particle shape classification for particles with sizes larger than 50 μm obtained from the CPI data (Figures 2d and 2h). The horizontal error bars represent the standard deviation of the cloud parameters highlighting significant horizontal inhomogeneities on a scale of 50 km.

[13] The cloud layers were entirely below the freezing level with temperatures ranging from −1°C to −12°C and with a temperature inversion located around 1000 m (see Figure 2d). The results show that the cloud consisted of mixed-phase layers throughout the sampled cloud depth.

[14] The cloud portions sampled during the descent of the aircraft from 1500 m to the cloud base are characterized by layers of large supercooled liquid water droplets with mean diameters Dm100 reaching 250 μm (Figure 2a). The vertical distribution of particle concentration remains nearly constant with a mean value N100 equal to 2 L^{-1} (Figure 2a). The presence of liquid water droplets is clearly evidenced by the LWC peaks (with values up to 0.4 g^{-3}) measured by the Nevzorov probe (Figure 2b). This is confirmed by the CPI particle shape classification which shows that large droplets account for more than 40% of the observed particles (with values up to 85% at 500 m) (Figure 2d). Additionally, the extinction coefficient derived from the PN data (Figure 2c) is correlated to the LWC measurements (with the square of the correlation coefficient, r^2, equal to 0.85) indicating that the optical properties of the cloud layers below 1500 m are mainly driven by water droplets. This statement is confirmed by values of the asymmetry factor g larger than 0.835, typical of layers dominated by liquid water droplets [*Gayet et al.*, 2002a; *Garrett et al.*, 2001]. The vertical variation of g in these layers can be explained by changes in the effective size of the droplets (proportional to the ratio LWC/σ_{ext}). In the cloud layers located above 1500 m, irregular shaped ice

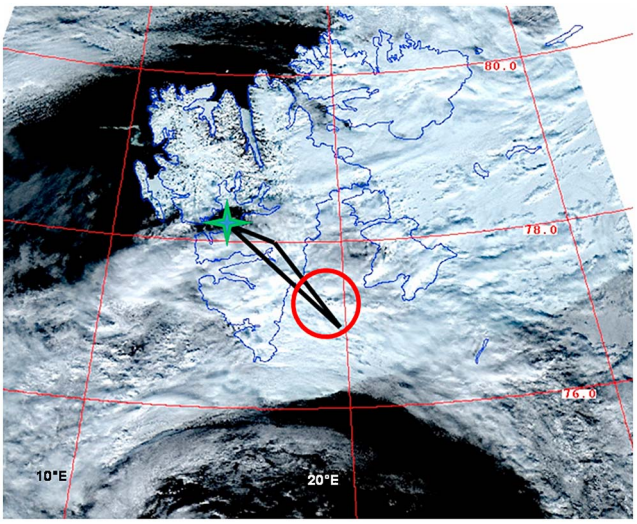

Figure 1. MODIS RGB true color composite satellite image taken on 21 May 2004 at 1010 UTC. The Polar 2 flight trajectory during the ASTAR campaign is superimposed on the map of the Svalbard Archipelago (thick solid line). The measurements discussed in this paper are located in the region defined by the red circle. The green symbol corresponds to the location of the Longyearbyen airport.

crystals account for more than 70% of the observed shapes (Figure 2d). Small fractions of columns (15%) and plates (9%) are also evidenced at 1950 m and 2500 m, respectively. The liquid water fraction, LWC/(LWC+IWC), gradually decreases with height and is associated with a decrease of the asymmetry factor from 0.84 to 0.81 characteristic of mixed-phase conditions (Figure 2b and Figure 2c). A similar trend was observed previously by *Garrett et al.* [2001] who found evidence that values of g within Arctic stratus decrease linearly with the fractional number of particles in the cloud that are ice rather than liquid.

[15] The cloud layers corresponding to the ascending track of the airplane are characterized by the presence of a significant ice phase. Larger concentrations of ice crystals (up to 15 L^{-1}) with Dm100 close to 280 μm are encountered (Figure 2e) at 1450 m and 1950 m. In these layers, the IWC is significant (50 $mg.m^{-3}$) and becomes higher than the LWC measured at 1950 m (30 $mg.m^{-3}$), resulting in asymmetry factor values approximately equal to 0.775 (Figures 2f and 2g). This means that the scattering properties of the cloud layers are essentially dominated by ice crystals. Accordingly, CPI measurements reveal a high occurrence of irregular shaped ice crystals accounting for 55% to 65% of the observed shapes (Figure 2h). Previous measurements have also shown that regular ice crystals are rare in Arctic clouds (the majority of ice crystals are irregular) due to altering processes and coagulation [*Korolev et al.*, 1999]. An interesting feature is the significant occurrence (30% to 40%) of needle or column shaped particles at 1450 m and 1950 m. In the upper cloud layers (at 2450 m and 2950 m) where the temperature is below −8°C, plates and stellars are the dominant habits among the regular shapes. The asymmetry parameter values are larger than 0.80 possibly due to the increase of the liquid water fraction (decrease of IWC and increase of LWC) or to the changes in ice crystal habits (increase of the fraction of irregulars and plates associated with a decrease of the fraction of column shaped crystals).

[16] The main conclusions based on the analysis of the measured profiles must be regarded with caution as no direct measurements of the microphysical properties of small water droplets (with sizes lower than 50 μm) were performed during this flight (the FSSP-100 probe was not available during this flight). This hinders the accurate interpretation of the coupling between microphysical and optical properties of the mixed-phase cloud system. Nevertheless, the large variability of ice crystal habits and liquid water fractions encountered in the cloud system gives the opportunity to study the relationships between the ice crystal shapes and their scattering properties. In section 3, we will investigate the impact of ice crystal shapes and liquid/ice partitioning on cloud optical properties in mixed-phase conditions.

3. Statistical Analysis of the Mixed-Phase Cloud System Optical Properties

3.1. Principal Component Analysis Methodology

[17] In this section, the principle component analysis (PCA) technique is applied to the polar nephelometer (PN) measurements following the methodology described by *Jourdan et al.* [2003a]. The PN optical database consists of approximately 2500 angular scattering coefficients relative to different particle microphysical properties. The main objective of the PCA is data reduction in order to allow a better physical interpretation of the mixed-phase cloud light-scattering properties. The PCA is designed to generate a new limited set of uncorrelated parameters, called principal components, representative of the original data set variability. We recall that the PN measures the angular scattering coefficients (ASC) $\overrightarrow{\sigma(\theta)}$ (i.e., nonnormalized scattering phase function) of an ensemble of randomly oriented particles as a function of 32 light-scattering directions θ ranging from 15° to 162°. According to the PCA technique, the jth measurement of angular scattering coefficients $\overrightarrow{\sigma_j(\theta)}$, expressed in log scale, can be expanded using the following expression:

$$\overrightarrow{\ln \sigma_j(\theta)} \simeq \left\langle \overrightarrow{\ln \sigma(\theta)} \right\rangle + \sum_{l=1}^{4} C_{jl} \overrightarrow{\xi_l(\theta)}, \qquad (1)$$

where $\langle \overrightarrow{\ln \sigma} \rangle$ represents the average ASC of the data set (i.e., the 2500 PN measurements). $\overrightarrow{\xi_l(\theta)}$ is the lth eigenvector (i.e., principal component) of the total data set correlation matrix. $C_{jl} = (\overrightarrow{\ln \sigma_j} - \overrightarrow{\langle \ln \sigma \rangle})^T$. $\overrightarrow{\xi_l}$ is the expansion coefficient corresponding to the lth eigenvector and the jth measurement vector $\overrightarrow{\ln \sigma_j}$.

[18] A first implementation of the PCA was used to detect data corresponding to unreliable photodiodes characterized by a low signal-to-noise ratio (eight were detected in the data set) or defective records during the measurements. After excluding the unreliable data, the PCA was applied a second time to the remaining set of measured ASC now documented on 24 scattering angles ranging from 15° to 155°. The first four eigenvectors, $\overrightarrow{\xi_l(\theta)}$ of the correlation matrix along with their normalized eigenvalues, λ_l, are displayed in Figure 3. The first eigenvector $\overrightarrow{\xi_1(\theta)}$ is

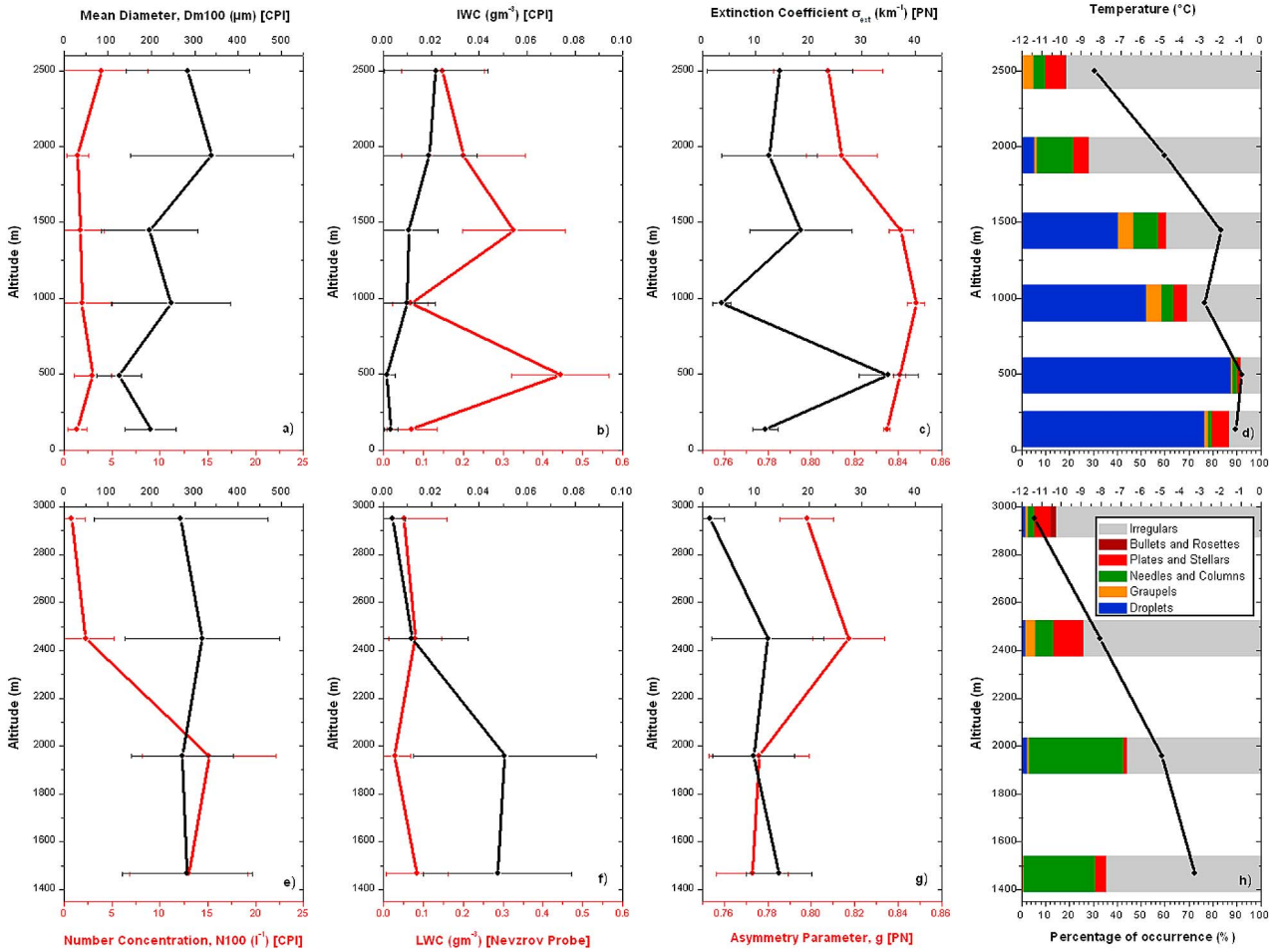

Figure 2. Average vertical profiles of microphysical and optical properties measured on April 21st during ASTAR 2004. The error bars correspond to the standard deviation of the cloud parameter at a given altitude. (a–d) The descending profiles. (e–h) The ascending profiles. Instruments selected to derive the cloud properties are indicated in brackets. Profiles of the number particle concentration N100 (red line) and mean diameter Dm100 with diameter greater than 100 μm (black line) measured by the CPI (Figures 2a and 2e). Profiles of liquid water content (LWC) obtained from the Nevzorov probe (red line) and ice water content (IWC) measured by the CPI (black line) (Figures 2b and 2f). Profiles of the asymmetry parameter (g) (red line) and the extinction coefficient σ_{ext} (black line) derived from the polar nephelometer (Figures 2c and 2g). Vertical profile of shape classification of particles larger than 50 μm in percentage weighted by concentration from CPI images (Figures 2d and 2h). Ice crystal habits are color coded. The average air temperature profile is superimposed with a black line.

approximately constant and represents 93.7% of the total variance. A constant eigenvector with scattering angle means that only the magnitude of the ASC varies without any changes in its global shape. This means that nearly 94% of the angular scattering intensity variations are related to changes of total cloud particle scattering or extinction (since the particle absorption is very low at 0.8 μm). Indeed, measurements show that there is a high correlation ($r^2 = 0.90$) between the first principal component and the extinction coefficient.

[19] The second eigenvector, $\overrightarrow{\xi_2(\theta)}$, accounts for nearly 6% of the ASC variability. $\overrightarrow{\xi_2(\theta)}$ reverses sign twice at scattering angles equal to 60° and 130° and maximizes at 100°. Accordingly, the second principal component governs the redistribution of scattered energy from the angle interval (60–130°) to scattering angles lower than 60° and higher than 130°. Light-scattering modeling studies [see, e.g., *Saunders et al.*, 1998; *Yang and Liou*, 1996; *Doutriaux-Boucher et al.*, 2000; *Xie et al.*, 2009] show that the scattering properties of cloud particles in sideward angles, approximately between 60° and 140°, are sensitive to the particle shape structure and thermodynamic phase.

[20] The third and fourth components taken together represent only 0.16% of the variance which is negligible compared to the first two components. However, these eigenvectors contain some information in important scattering regions that are not sufficiently well described by the first two principal components. For example, $\overrightarrow{\xi_4(\theta)}$ has opposite signs for $\theta < 40°$ and $\theta > 100°$ and has maximum absolute values at $\theta = 15°$ and around the angle interval [130–140°]. Indeed, modeling studies [*Xie et al.*, 2006,

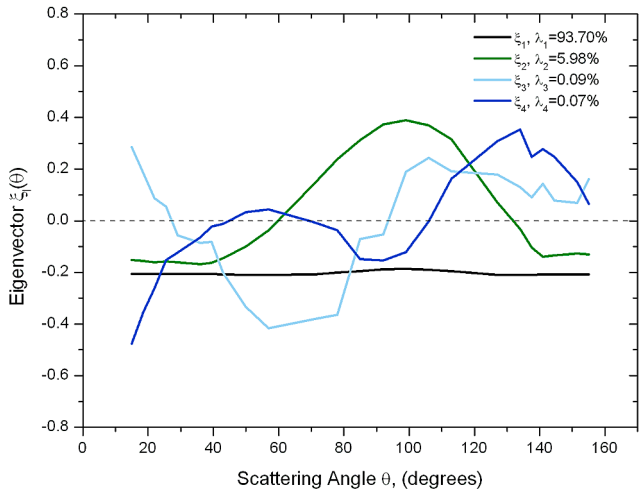

Figure 3. Results of the principal component analysis applied on the data set of measurements obtained with the polar nephelometer during the ASTAR flight. First four eigenvectors of the angular scattering coefficient (ASC) correlation matrix versus measured scattering angles. Values of the first four normalized eigenvalues of the eigenvectors are also displayed.

2009] show that the phase functions of ice crystals with different habits or surface roughness differ substantially around the 22° and 46° halo regions, at scattering angles around 140°, and at backscattering angles ($\theta > 120°$).

[21] The eigenvector analysis shows that nearly 99.9% of the ASC variability is described by the first four principal components. Consequently, each PN measurement can be expressed with a good accuracy as a linear combination of the four eigenvectors according to equation (1). Accordingly, the PN data are expanded and projected in the four-dimensional space of the expansion coefficient, C_{jl} (instead of the 24-dimensional space of ASC). The scatterplot of the $-C_{j2}$ expansion coefficient versus the C_{j4} coefficient describes the optical features of the cloud system in one of the clearest representations as evidenced in Figure 4. Each point can be directly associated with a nonnormalized scattering phase function (i.e., ASC) documented on 24 angles. Additionally, the ($-C_2$, C_4) coordinates of the average ASC of the data set are, in such representation, (0, 0).

[22] Figure 4 shows that the variability of C_{j2} coefficients is significant, with values approximately ranging from −1.25 to 1.25. According to the angular variation of $\vec{\xi_2(\theta)}$ displayed in Figure 3, large values of $-C_{j2}$ (i.e., $-C_{j2} > 0.75$) are associated to ASC characterized by low side scattering (60–130°) and higher scattering in the angular ranges (15–60°) and (130–155°). Additionally, positive values of $-C_{j2}$ are characterized by scattering regions where the concentration of points is high. This means that specific cloud regions sharing similar scattering properties can be identified on the basis of the second principal component. Moreover, this component is linearly correlated ($r^2 = 0.87$) to the measured values of the asymmetry parameter as evidenced on the expansion coefficient diagram (see color coded values of g in Figure 4). The asymmetry parameter increases with increasing values of $-C_{j2}$, reaching values larger than 0.83 for $-C_{j2} > 0.5$.

[23] In the space of the fourth principal component, the ASC are mostly distributed between −0.05 and 0.05. This means that most of the measured ASC do not significantly differ from the average ASC in the angular ranges (15–40°) and (100–155°). However, some specific scattering regions can be identified where values of C_{j4} are greater than 0.05 or lower than −0.05.

[24] Merging the information derived from the first four principal components, seven clusters representative of particular scattering behavior of cloud particles (see numbered areas in Figure 4) are determined. These clusters are mainly identified according to the C_{j2} coefficients and the concentration of points. Clusters 1 and 2 as well as cluster 6 and 7 are also discriminated on the basis of the fourth component. The first principal component enables us to select cloud segments on the base of their extinction coefficient values. Finally, the third component is used to refine the classification stemming from the fourth component.

[25] Table 1 summarizes the altitude, the static temperature, the asymmetry factor, and the extinction coefficient values associated with the different clusters identified in Figure 4. It can be clearly seen that most of the clusters are representative of specific cloud layers (altitude, temperature and optical properties). For instance, the ASC classified in clusters 1, 3, and 6 characterize the particle scattering behavior of the cloud system at approximately 500 m, 150 m, and 2950 m altitude, respectively. The cloud layers located between 950 m and 1450 m, characterized by large asymmetry factor values (0.85) and liquid water droplets, are gathered in cluster 2 ($-C_{j2} > 0.5$ and $C_{j4} < -0.05$). Cloud particles regrouped in cluster 7 ($-C_{j2} < 1$ and $C_{j4} > 0.05$) exhibit the lowest asymmetry parameter (0.765) and correspond to the ice crystal particles sampled during the ascending track of the aircraft between 1450 m and 1950 m. Cluster 4 ($0 < -C_{j2} < 0.5$ and $-0.05 < C_{j4} < 0.05$) and Cluster 5

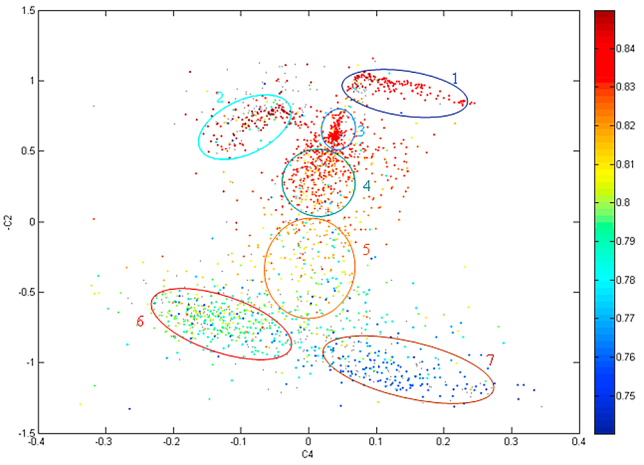

Figure 4. Expansion coefficient diagram: second coefficient versus fourth coefficient. The points are color coded according to their corresponding asymmetry parameter value shown in the color bar. The seven typical scattering regimes are indicated and numbered accordingly.

Table 1. Median Values of Altitude, Z, Temperature, T, Asymmetry Parameter, g, and Extinction Coefficient, σ_{ext}, Corresponding to the Seven Clusters Identified by the Principle Component Analysis[a]

	Z (m)		T (°C)		g PN		σ_{ext} PN (km^{-1})	
	Median	25th to 75th Percentiles	Median	25th/75th Percentiles	Median	25th to 75th Percentiles	Median	25th to 75th Percentiles
Cluster 1	494	492–495	−0.9	−1.0/−0.5	0.843	0.840–0.855	34.9	29.4–41.5
Cluster 2	970	969–1447	−1.7	−2.2/−1.3	0.849	0.848–0.852	4.5	2.1–8.9
Cluster 3	140	138–168	−1.2	−1.3/−1.2	0.838	0.835–0.839	15.0	11.7–16.5
Cluster 4	1943	1447–2500	−4.8	−7.9/−1.9	0.830	0.824–0.833	19.9	13.9–26.1
Cluster 5	2450	1943–2593	−8.0	−9.0/−4.9	0.808	0.801–0.815	12.4	3.7–20.8
Cluster 6	2771	2627–2950	−10.1	−11.3/−9.1	0.797	0.790–0.801	1.6	0.7–2.1
Cluster 7	1960	1465–1961	−4.8	−4.9/−3.7	0.765	0.755–0.776	8.9	4.6–13.6

[a]See Figure 4. The 25th to 75th percentiles are also indicated.

($-0.5 < -C_{j2} < 0$ and $-0.05 < C_{j4} < 0.05$) are associated with the cloud particles sampled between 1450 m and 2450 m. For these two clusters the scattering properties vary more significantly and do not really match with specific cloud regions evidenced during the flight track. However, as a whole, the cloud classification based on ASC measurements is consistent with the cloud layers properties derived from the airplane vertical profiles (e.g., Figure 2).

3.2. CPI-PN Synergy: An Attempt to Couple Ice Crystal Shapes to Optical Properties

[26] The averaged normalized phase functions related to the first four clusters identified by the PCA as well as the one of the whole data set are displayed in Figure 5 (left). These phase functions are characterized by substantial scattering at forward angles ($\theta < 60°$) that is associated with much lower scattering at sideward angles ($120° > \theta > 60°$) and enhanced scattering around 140° corresponding to the rainbow feature. This typical behavior reveals that the single-scattering properties of these clusters are mostly dominated by spherical particles (mainly water droplets). The histograms of cloud particle habits derived from CPI measurements shown in Figure 5 (right) confirm this statement. Large liquid water droplets (with diameter up to 500 μm) constitute more than 80% of the particles sampled in the cloud regions classified in clusters 1, 2 and 3.

[27] The main difference between the phase function behavior occurs in the side scattering region (60–130°). This is in complete agreement with the position of the four clusters on the expansion coefficient diagram (Figure 4). A decrease in the value of the expansion coefficient $-C_{j2}$ is associated to a side scattering enhancement. As mentioned in section 3.1 and in the study of *Jourdan et al.* [2003a] this scattering behavior can be connected in particular to changes of particle shape or composition (thermodynamic phase and liquid water fraction). This is clearly illustrated by the histograms of cloud particle habits relative to cluster 1 ($-C_{j2} > 0.8$) and cluster 4 ($0 < -C_{j2} < 0.5$). For cluster 1, 98% of particles with size greater than 50 μm are droplets whereas the area classification gives 4% droplets, 37% graupels, 20% irregulars and 13% columns for cluster 4. Even though the number concentration of cluster 4 is dominated by water droplets (70%), the phase function is mostly sensitive to the projected area of the particles (area

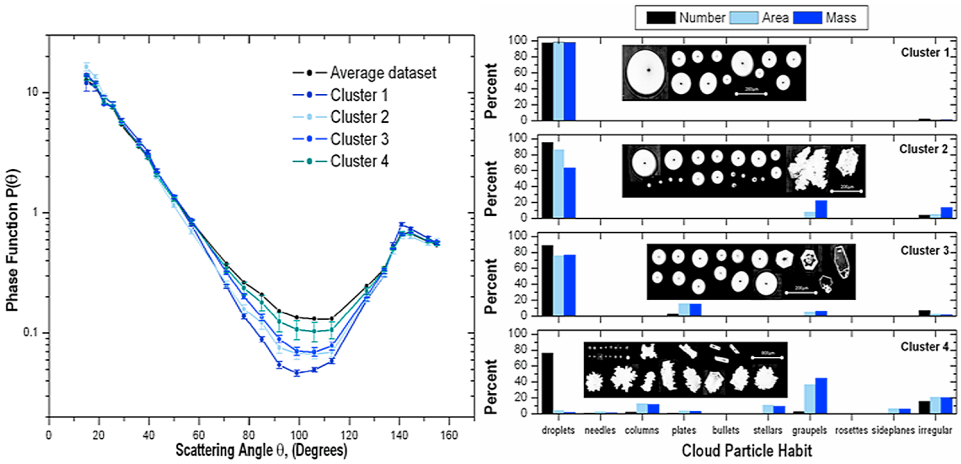

Figure 5. Scattering and particle habit properties of clusters 1, 2, 3 and 4 (the clusters are defined in Figure 4). (left) Average phase functions of the first four clusters determined by the PCA analysis. Variations of optical properties within each cluster are represented by means of standard deviation (bars). (right) Histogram of cloud particle habits derived from CPI measurements for the first four clusters. The percentages weighted by concentration, area and mass are shown for each habit category. Typical images of cloud particles observed by the CPI are also displayed for these clusters.

concentration). So, the side scattering enhancement observed in cluster 4 is more likely to be attributed to the presence of large non spherical ice crystals (mainly graupels and irregulars). This trend was already observed by *Gayet et al.* [2002a] for clouds in mixed-phase conditions. Additionally, the estimated liquid water fraction (LWF) derived from the CPI and the Nevzorov probe measurements is higher for cluster 1 (100%) than for cluster 4 (80%). However, the changes in the measured LWF cannot explain the fact that the phase functions of cluster 2 and 3 are more flat at side scattering angles than the one corresponding to cluster 1. LWF for clusters 2 and 3 is 99.7% and 98.7%, respectively. The differences of scattering properties are more likely to be due to the variability of particle shape and size although the contribution of undetected small water droplets cannot be excluded. Indeed, when sorted by area, the percentages are 86% droplets, 8% graupels and 5% irregulars for cluster 2 and 75% droplets, 15% plates and 5% graupels for cluster 3 compared to nearly 100% droplets for cluster 1.

[28] The phase functions associated with clusters 5, 6 and 7 as well as the corresponding histograms of cloud particle habits are displayed in Figure 6. In comparison to the previous scattering patterns (Figure 5), the phase functions exhibit a featureless behavior and are more flat at side scattering angles, which is in accordance with most of the observations in glaciated clouds [*Francis et al.*, 1999; *Shcherbakov et al.*, 2006; *Gayet et al.*, 2006; *Jourdan et al.*, 2003b; *Baran and Francis*, 2004]. The main differences between the phase function of cluster 5 and the average one occur in the side scattering region (60–130°) as expected by its location on the expansion coefficient diagram ($-0.5 < -C_{j2} < 0$ and $-0.05 < -C_{j4} < 0.05$) (see Figure 4). CPI measurements show that irregularly shaped ice crystals account for more than 90% of the particle area observed in the cloud layers gathered in cluster 5. However, when sorted by number, the contribution to total concentrations is nearly 40% for irregularly shaped crystals and 50% for water droplets. This means that this cluster is characterized by a mixture of water droplets (with sizes significantly smaller than the ones observed in cluster 1, 2 and 3) and large rimed ice crystals. In this sense, the particle composition of cluster 5 and cluster 4 is similar but the fractional contribution of ice crystals to optical extinction is more pronounced in cluster 5.

[29] The phase functions corresponding to cluster 6 and 7 deviate from the data set average phase function at nearly all scattering angles. This is particularly true in the side scattering region but also at backward angles where the phase function is more flat (the rainbow feature disappears). CPI measurements show that these two clusters are characterized by the presence of specific ice crystals habits (stellars, sideplanes, columns and needles) which were not identified in the other clusters. Particles with a predominant *a*-axis growth (54% stellars and 22% complex with sideplanes for percentages by area) are gathered in cluster 6 whereas a predominant *c*-axis growth (45% columns and needles) is observed for cluster 7. This variability of ice crystal shapes can be related to the significant discrepancies observed in the angular scattering region (100–155°). As mentioned earlier, *Xie et al.* [2006 and 2009] showed that the phase functions of different ice crystal habits differ substantially in this region and that surface roughness or the inhomogeneity inside the ice crystal leads to a featureless and flat behavior for scattering angles greater than 100°. This ties in with the position of cluster 6 and 7 in the expansion coefficient diagram as the fourth principal component has maximum values for $\theta > 100°$. In this region, light is scattered more efficiently by the cloud particles gathered in cluster 7 resulting in higher values of C_{j4} ($C_{j4} > 0.05$).

[30] The main conclusion of this section is that the representative optical patterns revealed by the principal component analysis are consistent with the particle habit classification derived from the CPI measurements. Thus, the synergy between the CPI and PN can be exploited to link the microphysical and shape properties of cloud particles to their single-scattering properties. Indeed, we find that the general behavior of the phase function is connected to specific ice crystal habits. A limitation of this study is that the optical contribution of small particles with sizes smaller than 50 μm is not considered due to ambiguity in habit identification for smaller CPI particle images. In essence, we are assuming that, either smaller particles contribute negligibly to total extinction (which is unlikely) or that habit distributions are approximately invariant with size (which is plausible). We discuss this issue further in section 4.

4. Discussion of the Assessment of Equivalent Microphysical Models

[31] This section is devoted to the assessment of equivalent microphysical models capable of describing the optical properties of ice crystals in the mixed-phase cloud. To this end a key issue is to evaluate the contribution of small particles to the measured scattering properties obtained from the PCA and the PN data. To study this issue, the iterative inversion method, developed by *Oshchepkov et al.* [2000], using light-scattering modeling is applied to the average ASC within a given cluster. The method is based on a bicomponent representation of cloud composition and constitutes a nonlinear weighted least square fitting of the ASC using positive and smoothness constraints on the desired particle size distribution [see *Oshchepkov et al.*, 2000; *Jourdan et al.*, 2003b]. It is designed for the retrieval of two volume particle size distributions simultaneously. For each component, the thermodynamic phase is fixed but the shape of the cloud particles does not necessarily remain invariant for all sizes within a particle size distribution. The shape of the particle is prescribed among the following habits: spheres, droxtals, columns with four aspect ratios (1, 2, 5, 10), plates with three aspect ratios (0.1, 0.5, 0.2), hollow columns, six branch bullet rosettes and aggregates of columns. The surface texture or roughness of the ice crystals is also considered by assuming small tilted facets on the ice crystal surface [*Yang and Liou*, 1998]. The slopes of the tilted facets are randomly sampled based on the following Gaussian distribution [*Cox and Munk*, 1954; *Yang et al.*, 2008a],

$$f(s) = \frac{1}{\sigma\sqrt{\pi}} \exp\left(-\frac{s^2}{\sigma^2}\right), \tag{2}$$

where s represents the slope of the tilted facets and σ is relative to the variance of the distribution. Thus, the surface of the ice crystal can vary from smooth to deeply rough

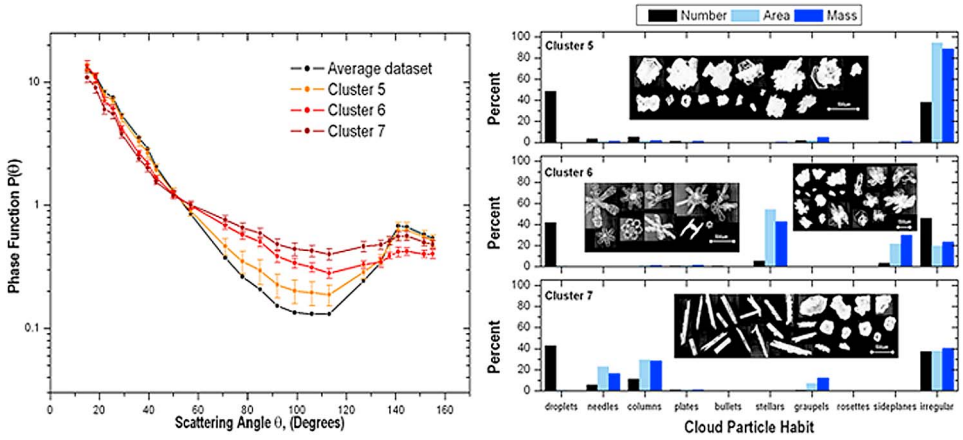

Figure 6. Same as Figure 5 but for clusters 5, 6, and 7.

when σ increases from 0 to 1. In the simulations, the surface texture of the ice crystals is accounted for by considering three roughness parameters: smooth (σ = 0), moderately rough (σ = 0.025) and deeply rough (0.25). These values are consistent with the ones used in a previous study on the impact of ice particle roughness on the scattering phase matrix by *Baum et al.* [2010]. Detailed information on the ice crystal surface roughness and the computation of the scattering properties for surface roughened ice crystals have been thoroughly introduced by *Yang et al.* [2008a, 2008b] and *Shcherbakov et al.* [2006].

[32] The retrieval algorithm is based on a lookup table approach where the ASC of individual cloud particles need to be specified. Accordingly, the optical properties of spherical particles with diameters ranging from 2 μm to 500 μm are simulated using the Lorentz-Mie theory. The scattering patterns of nonspherical randomly oriented in 3D space ice crystals are computed by the improved geometric-optics model developed by *Yang and Liou* [1996]. The calculations are performed for particles with maximum dimensions ranging from 2 μm to 200 μm for droxtals and from 20 μm to 900 μm for the other ice crystal habits.

[33] The retrieved ASC from the inversion scheme along with the direct PN measurements corresponding to the first four clusters are displayed in Figure 7. The retrievals are in good agreement with the measurements even though discrepancies are encountered near the rainbow scattering region for $\theta > 140°$. Such measured enhanced scattering has already been observed when light reflected on the edges of the forward positioned photodiodes $\theta < 15°$ contaminates the light scattered toward the backward positioned photodiodes $\theta > 140°$.

[34] The minimum root-mean-square deviation (RMSD) between the measured (represented by dots in Figure 7) and the retrieved ASC (gray line) were achieved for a microphysical model corresponding to a combination of water droplets and deeply rough droxtal shaped ice crystals (with roughness parameter equal to 0.25). It should be noted that the habit classification of CPI images is unambiguous only when ice particles have sizes larger than about 50 μm. Therefore, they can only be used as a priori information on the general growth mode of the particles or to characterize the deviation from pristine particles (riming or evaporation on the edges of the crystal). In this respect, deeply rough droxtal particles must be considered as surrogate for small irregular ice crystals.

[35] Considering the discrepancies observed at scattering angles larger than 140°, the RMSD gave acceptable values of 22%, 18%, 16%, and 12% for clusters 1, 2, 3, and 4, respectively. The contribution of each microphysical component (dashed lines in Figure 7) emphasizes that water droplets dominate the scattering phase function for each of the 4 clusters. Indeed, droplets contribute for more than 99% of the total extinction (or scattering) coefficient for clusters 1, 2 and 3. For these clusters, the ice particle scattering contribution is negligible and the sensitivity of the inversion results regarding the shape or the roughness of the crystals is very low. However, for cluster 4, the ice contribution becomes significant representing 7.5% of the total scattering. Here droxtal shaped particles are responsible for the enhanced side scattering observed in the measurements. Figure 7 also shows the asymmetry factors corresponding to the retrieved ASC. Compared to the measured asymmetry parameters listed in Table 1, the retrieved values of g are consistent but larger. In the retrievals, g is inferred from the scattering phase function documented between 0° and 180° whereas the measured g is approximated based on an incomplete phase function (between 15° and 155°). The retrieved values clearly indicate that cluster 1 (g = 0.864) is characterized by larger water droplets than clusters 2 and 3 (g = 0.854 and g = 0.847). Whereas, the lower asymmetry factor observed for cluster 4 (g = 0.835) is more likely to be explained by an enhanced side scattering associated with a non negligible population of ice crystals.

[36] The bulk microphysical parameters retrieved by the inversion scheme are presented in Table 2 along with the direct measurements performed by the CPI and the Nevzorov probe. Taking into account the instrumental errors associated with the Nevzorov probe (at least 15% for LWC), the retrieved liquid water contents are in reasonable agreement with the measurements. However, the retrieved LWC of cluster 2 is underestimated, probably because the contribution of large droplets is also underestimated in the inversion. Indeed, this cluster is characterized by a low extinction coefficient (4.5 km^{-1}; see Table 1) and a relatively high LWC (0.105 $g.m^{-3}$) which indicate that a small concentration of

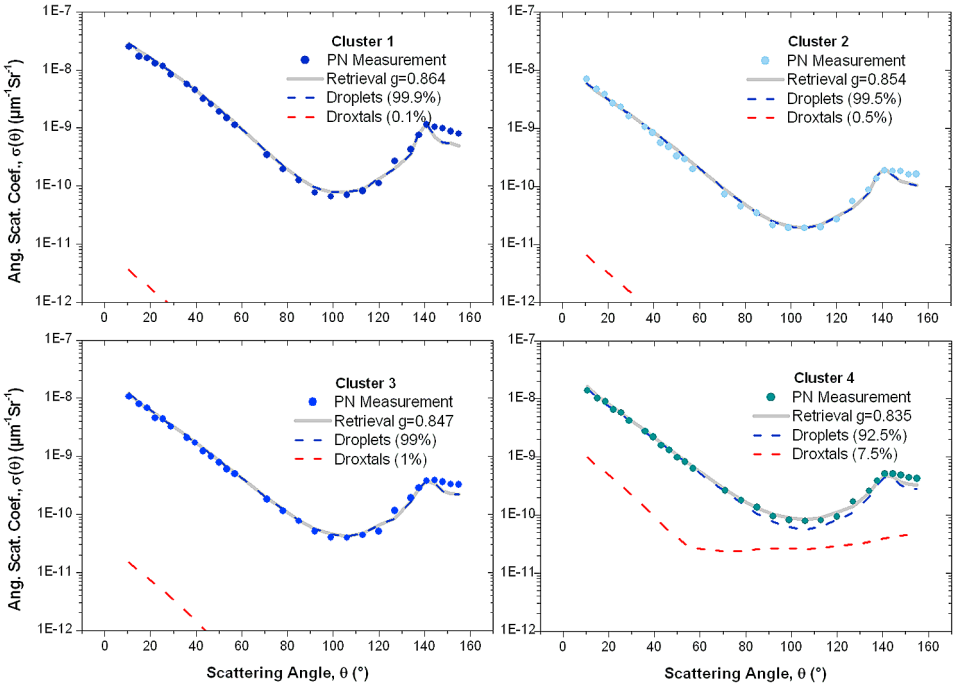

Figure 7. Measured and retrieved angular scattering coefficients at the polar nephelometer nominal wavelength (800 nm) for clusters 1, 2, 3, and 4. The contributions of both components (water droplets and ice crystals) to the total scattering properties are also displayed. The ice crystal component used in the retrievals is constituted of deeply rough droxtals with roughness parameter equal to 0.25 and maximum dimension ranging from 2 μm to 200 μm.

large droplets may be responsible for most of the scattering. But, the problematic accuracy of the LWC inferred from the Nevzorov probe for optically thin liquid water clouds cannot be excluded from consideration. For each cluster, retrievals compare well with measurements, indicating that the IWC is negligible compared to the LWC. The liquid water fraction reaches more than 99.9% for cluster 1 decreasing to approximately 80% for cluster 4. Measurements confirm that these four cloud patches are dominated by liquid water droplets.

[37] Table 2 also displays the retrieved concentration and effective diameter of cloud particles corresponding to the water droplet component and the ice crystal component. For these parameters, direct measurements and retrievals are not quantitatively comparable as the CPI measurements are only valid for particles typically larger than 50 μm. The retrieved concentration for the water droplet component ranges between 37 cm^{-3} for cluster 2 to 163 cm^{-3} for cluster 4 which is 3 orders of magnitude more than the CPI measurements. However, the concentrations of both water droplets and ice crystals assessed from the PN measurements are in the range of previous observations performed in mixed-phase Arctic clouds [*McFarquhar et al.*, 2007; *Ehrlich et al.*, 2008]. The study of *McFarquhar et al.* [2007] focused on single-layer mixed-phase stratocumulus and showed that the cloud droplet and the ice crystal concentrations were on average 44 ± 30 cm^{-3} and 0.3 ± 1.8 cm^{-3}, respectively. Additionally, Table 2 reveals that the retrieved and measured concentrations of particles with sizes greater than 50 μm (N50) are in reasonable agreement. Values range from 2 L^{-1} for cluster 3 to 95 L^{-1} for cluster 4. Finally, water droplets with diameter lower than 50 μm contribute to more than 98.5% of the total scattering signal of the water droplet component. The small ice crystal contribution always exceeds 63%. These results confirm that the cloud layers corresponding to the first four clusters are optically dominated by particles (mainly water droplets) with sizes lower than 50 μm.

[38] The retrieved and measured ASC corresponding to cluster 5, 6 and 7 are represented in Figure 8 (cluster 4 is also displayed for comparison). The results show that the retrievals and the measurements are in good accordance with RMSD approximately equal to 9.5%, 7%, and 10% for clusters 5, 6, and 7, respectively. The best fit of the measurements for cluster 5 was achieved with a microphysical model representing a combination of water droplets, deeply rough columns (with aspect ratio equal to 1 and with roughness parameter equal to 0.25) and aggregates of columns. For cluster 6, it was found that an ensemble model of deeply rough plates with aspect ratios of 0.5 and 0.1 was the best to reproduce the scattering properties of the ice crystals. Finally, a mixture of deeply rough hexagonal columns (with roughness parameter equal to 0.25) with varying aspect ratios was used to model the ice crystal component of cluster 7.

[39] The contribution of each microphysical component reveals that an ensemble of rough ice crystals reproduces the general featureless and flat (mainly at side scattering angles) behavior of the measurements. Indeed, in the simulation the roughness of the ice surface is assumed to be composed of a number of small facets which are locally planar and randomly tilted from position corresponding to the case of a perfectly plane surface. The rough surface can substantially

Table 2. Measured and Retrieved Bulk Microphysical Properties for Clusters 1, 2, 3, and 4[a]

	Droplets and Crystals	Water Droplets	Ice Crystals	Measurements D > 50 μm
		Cluster 1, RMSD = 21.7%		
N (L^{-1})	61,863	61,823	40	150
N50 (L^{-1})	61.3	61	0.3	39
TWC (mg m^{-3})	414.6	414.5	0.1	421(LWC)+0.1(IWC)
TWC50	9.3	9.2	0.1	
D_{eff} (μm)	28	28	55	54
D_{eff}50	67	67	118	
		Cluster 2, RMSD = 18.3%		
N (L^{-1})	37,626	37,583	43	28
N50	19.5	19	0.5	3
TWC (mg m^{-3})	61.4	61.2	0.2	105(LWC)+0.3(IWC)
TWC50	3.3	3.2	0.1	
D_{eff} (μm)	22	21	60	48
Deff50	71	69	117	86
		Cluster 3, RMSD = 16.2%		
N (L^{-1})	94,811	94,734	77	10
N50	2	0.3	1.7	4
TWC (mg m^{-3})	83.9	83.4	0.5	77(LWC)+1(IWC)
TWC50	0.4	0.04	0.36	
D_{eff} (μm)	15	15	62	20
Deff50	109	66	117	135
		Cluster 4, RMSD = 11.8%		
N (L^{-1})	166,660	163,420	3232	151
N50	96	1	95	45
TWC (mg m^{-3})	119.5	91.9	27.6	91(LWC)+22.5(IWC)
TWC50	14	0.1	13.9	
D_{eff} (μm)	17	14	52	61
Deff50	94	67	94	

[a]The measured microphysical properties correspond to the direct measurement performed by the CPI (for N, IWC, and D_{eff}) and the Nevzorov probe (for LWC). The retrieved properties are assessed using the PN measurements.

affect the scattering properties by reducing the backscattering signal and smooth out the scattering peaks linked to the hexagonal geometry of the "idealized" modeled ice crystals. However, a water droplet component is still needed to model the slight scattering enhancement observed for $\theta > 120°$ as well as to more accurately fit the scattering behavior for $\theta < 60°$. Moreover, in his review paper, *Baran* [2009] highlighted that an ensemble model of ice particles or inhomogeneous crystals is more suitable to represent the scattered intensity of glaciated clouds than a single pristine ice crystal model. Our retrievals show that this seems to be the case for mixed-phase clouds when the liquid water fraction is lower than approximately 55%.

[40] Ice crystals contribute for 26% of the total scattering coefficient for cluster 5 and reach 86.5% for cluster 7. Even though the retrieved asymmetry parameters are slightly higher than the ones directly derived from the PN measurements, the trends are still respected. The larger the ice crystals contribution to the scattering properties of the cloud patches, the lower is *g*. This stems from the behavior of the ASC in the side scattering region which is partly connected to the liquid water fraction. Indeed, the mean ASC of cluster 5 is less flat at side scattering compared to the ASC of cluster 6 and 7 resulting in higher asymmetry parameters (0.812, 0.799, and 0.775, respectively). As reported in Table 3, this feature could be explained by a retrieved liquid water fraction (55%) 10 times higher than the ones associated with cluster 6 and 7 (5.5%). On the other hand, the difference of the *g* values between cluster 6 and 7 is more likely to be explained by the differences in the retrieved ice crystal habits.

[41] The results of the inversion displayed in Table 3 show that the retrieved and measured liquid water content are in close agreement. This is generally true for the IWC even though the retrievals are overestimated by a factor of 2 for cluster 7. The only microphysical model which did not lead to a significant overestimation of the IWC was a mixture of water droplets and rough aggregates of columns. However, the use of such model to fit the measured ASC resulted in an unrealistically high concentration (29 cm^{-3}) of small ice crystals with maximum dimensions smaller than 25 μm (i.e., with an effective diameter D_{eff} = 8 μm). Accordingly, we selected an ensemble model composed of deeply rough hexagonal columns in order to reproduce the scattering properties observed in cloud segments gathered in cluster 7. With this model, the retrieved concentrations (8.6 cm^{-3}) and effective sizes (44 μm) of the ice crystals are more in accordance with previous observations [see *McFarquhar et al.*, 2007].

[42] As a whole, the retrieved concentrations are at least 3 orders of magnitude higher than the measurements for each cluster. The water droplet component dominates the ice crystal component in number concentration but this is not the case when comparing the volume concentration. Indeed, the IWC contributes to nearly 45% of the total water content for cluster 5 and 95% for clusters 6 and 7. As evidenced by the retrievals of the concentration of particle with size larger than 50 μm (N50) and of the effective sizes (D_{eff}), higher concentrations of large ice crystals are evidenced in these cloud layers compared to those corresponding to clusters 1, 2 and 3. Additionally, the retrieved values of N50 are in

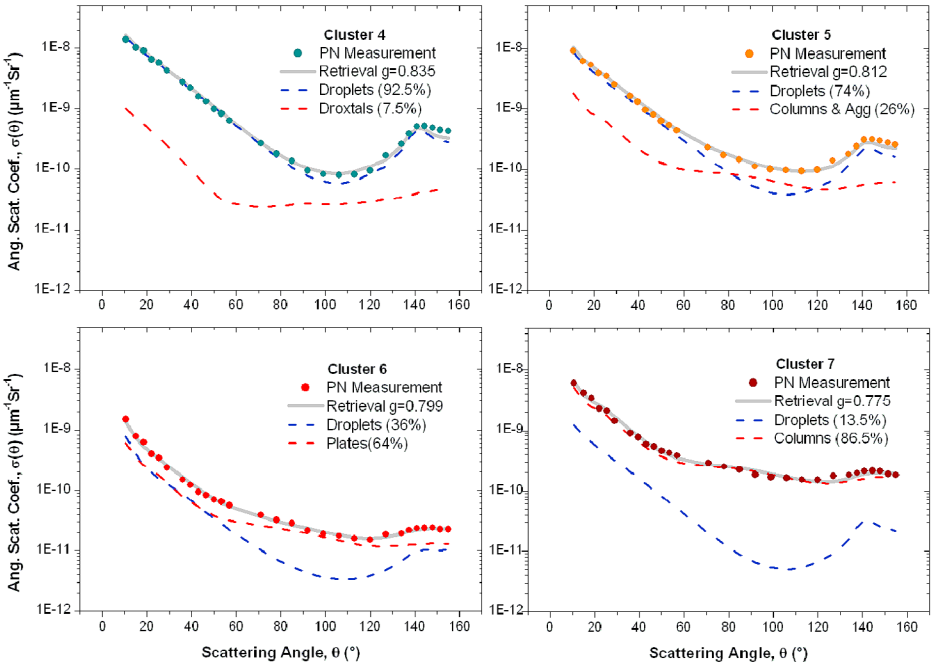

Figure 8. Same as Figure 7 but for clusters 4, 5, 6, and 7. The ice crystal component used in the retrievals is: for cluster 5 a combination of deeply rough columns with roughness parameter equal to 0.25, aspect ratio 1, maximum dimension ranging from 20 μm to 330 μm and deeply rough aggregates with maximum dimension ranging from 330 μm to 900 μm; for cluster 6 a combination of deeply rough plates with roughness parameter equal to 0.25, aspect ratio 0.5, maximum dimension ranging from 20 μm to 330 μm and deeply rough plates, aspect ratio 0.1, with maximum dimension ranging from 330 μm to 900 μm; for cluster 7 a combination of deeply rough columns with roughness parameter equal to 0.25, aspect ratio 1, maximum dimension ranging from 20 μm to 330 μm and deeply rough columns, aspect ratio 5, with maximum dimension ranging from 330 μm to 900 μm.

much better agreement with measurements than are total concentrations. The acceptable match between the retrieved and CPI derived ice crystal effective diameters is most likely explained by the accurate retrieval of IWC. Values are similar to those found previously by *McFarquhar et al.* [2007] (i.e., 50 ± 4 μm). However, our retrieval shows that ice crystals with sizes smaller than 50μm account for more than 96% of the total ice number concentration of each cluster. Finally, we get better insight into the optical importance of small ice crystals by estimating their influence on the total scattered signal. Crystals with sizes lower than 50 μm contribute to 94%, 51%, and 84% of the scattering coefficient of the cloud layers corresponding to clusters 5, 6, and 7, respectively. This ties in with the studies of *Yang et al.* [2003] and *Zhang et al.* [2004] where it was found that the single-scattering properties of glaciated clouds are highly sensitive to the presence of small ice crystals (with size parameter lower than 20 μm).

[43] To summarize the above, the inversion results confirm that the use of idealized geometric shape models representing ensembles of rough ice crystals combined with a population of water droplets is suitable to describe the scattering properties of the mixed-phase cloud. Such a mixture of shapes is able to represent the bulk LWC and IWC derived from in situ CPI measurements. However, the retrieved concentration deviate from measurements and there are at least two possibilities to explain these discrepancies.

[44] First, the inverse problem might be ill posed meaning that for one specific combination of ice crystal geometry different size distributions can be retrieved. In this respect, the inversion algorithm was designed to minimize the root-mean-square deviation between the measured and the retrieved ASC. In the set up of the inversion procedure, priority was given to retrieve LWC and IWC in order to fit as best as possible to the measurements. Additionally, a priori information on the ice crystal habit and liquid water fraction were established from the CPI and Nevzorov probe observations. For each cluster, several combinations of shapes were tested and the ensemble model corresponding to the minimum RMSD and to the best retrieval of IWC and LWC according to the measurements was selected. However, for a given RMSD and a given cluster, the maximum variability of the retrieved concentration, effective size and TWC caused by changes in the microphysical model are 75%, 50%, and 35%, respectively, for the water optically dominated clusters. For the clusters where the ice crystals are responsible for most of the scattering properties (clusters 6 and 7), the discrepancies are 140%, 80%, and 75% for the concentration, effective size, and TWC, respectively. Additionally, the impact of the roughness parameter on these retrieved quantities can be significant. Table 4 along with Figure 9 shows an example of the influence of ice crystal roughness on the retrievals. There, the microphysical model is the same as the one obtained for cluster 7 except for the values of the ice particle roughness parameter.

Table 3. Measured and Retrieved Bulk Microphysical Properties for Clusters 5, 6, and 7[a]

	Droplets and Crystals	Water Droplets	Ice Crystals	Measurements D > 50 μm
		Cluster 5, RMSD = 9.5%		
N (L^{-1})	165,960	162,820	3130	50
N50	22	3	19	18
TWC (mg m^{-3})	70.1	38.7	31.3	37.2(LWC)+25(IWC)
18	4.5	0.7	3.8	
D_{eff} (μm)	16	11	27	25
Deff50	72	70	72	70
		Cluster 6, RMSD = 6.7%		
N (L^{-1})	30,286	29,556	730	31
N50	30	0.5	29.5	8
TWC (mg m^{-3})	17.2	1.1	17.1	1(LWC)+11(IWC)
TWC50	14	0.5	13.5	
D_{eff} (μm)	37	7	50	52
Deff50	83	68	83	103
		Cluster 7, RMSD = 9.7%		
N (L^{-1})	29,142	20,553	8589	67
N50	86	3	83	23
TWC (mg m^{-3})	149	8	141	10(LWC)+ 70(IWC)
TWC50	88	1	87	
D_{eff} (μm)	41	15	44	61
Deff50	160	75	160	175

[a]The measured microphysical properties correspond to the direct measurement performed by the CPI (for N, IWC, and D_{eff}) and the Nevzorov probe (for LWC). The retrieved properties are assessed using the PN measurements.

It can be clearly seen that the discrepancies between the retrieved microphysical properties are significant. For example, if moderately roughened ice columns (σ = 0.025) are considered instead of deeply rough (σ = 0.25) ice particles, the effective size and the TWC can be underestimated by a factor 2. In this particular case, the TWC retrieved with the moderately rough ice crystals model would be in better agreement with the direct measurements. However, Figure 9 shows that the best fit of the measured ASC is achieved with the deeply rough ice particle model with a RMSD equal to 9.7% (compared to 17.3% and 25% for moderately rough and smooth crystals, respectively). Indeed, deeply rough particles tend to smooth out maxima of the phase function linked to the hexagonal geometry of the ice columns. This leads to an ASC with a featureless and flat behavior which is more in accordance with the measurements.

[45] Second, we have found that it is not possible to reproduce the measured scattering properties of the cloud patches using light-scattering modeling based exclusively on CPI observations. This strengthens the theory that CPI information should be considered with caution and should mainly be used to characterize the ice particle growth mode and to derive the bulk microphysical properties of large ice crystals only (with dimensions larger than 50 μm). However, it is also possible that the discrepancies between retrievals and measurements are caused by the shattering of large ice crystals with diameters larger than 100 μm on the shrouded inlets of the CPI and PN probes [*Korolev and Isaac*, 2005]. *Heymsfield* [2007] and *McFarquhar et al.* [2007] found that particle shattering results in a subsequent enhancement of the total concentration of ice crystals especially for sizes lower than 50 μm. *Shcherbakov et al.* [2010] showed, with a probabilistic model, that for a size distribution of ice crystals with an effective diameter equal to 70 μm (and with 10 μm fragments of ice crystals) the extinction coefficient derived from the PN could be overestimated by 25%. The values of the asymmetry parameter estimated using the PN measurements are also likely to be reduced by non pristine small ice particles produced by the shattering of larger ice crystals on the probe tip. Indeed, light-scattering modeling shows that a decrease of the size of the ice crystals coupled with an increase of their surface roughness leads to a decrease of the asymmetry parameter [*Baum et al.*, 2010]. However, with the instrument payload onboard the aircraft, it was not possible to evaluate accurately possible effects of shattering artifacts on measured ice crystal concentrations. New particle imaging probes with high pixel resolution (2D-S or CIP for example) may be used to quantify the contribution of shattering to particle size distribution and optical properties [*Lawson et al.*, 2006].

Table 4. Example of the Impact of Ice Particle Roughness on the Retrieval of Bulk Microphysical Properties[a]

	Model With Smooth Ice Crystals	Model With Moderately Rough Ice Crystal	Model With Deeply Rough Ice Crystals	Measurements
N (L^{-1})	200,460	126,090	29,142	67
TWC (mg m^{-3})	42	71	149	10(LWC)+ 70(IWC)
D_{eff} (μm)	14	20	41	61

[a]The results are relative to cluster 7; that is, the microphysical model used in the inversion is a combination of water droplets and ice columns with varying aspect ratio. Three different surface roughness of the ice crystals are considered in the inversion process: smooth (σ = 0), moderately rough (σ = 0.025), and deeply rough (σ = 0.25).

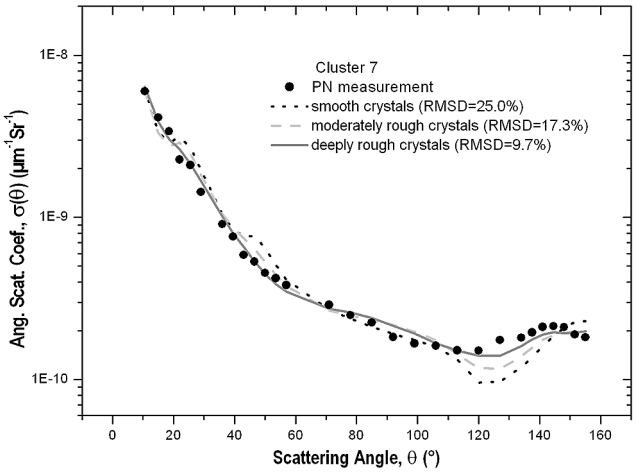

Figure 9. Example of the impact of the ice particle roughness on the retrieval of angular scattering coefficients. The results are relative to cluster 7; that is, the microphysical model used in the inversion is a combination of water droplets and ice columns with varying aspect ratio. Three different surface roughness of the ice crystals are considered in the inversion process: smooth ($\sigma = 0$), moderately rough ($\sigma = 0.025$), and deeply rough ($\sigma = 0.25$). The root-mean-square deviation (RMSD) from the measurements is also displayed.

Additionally, the accurate assessment of the number concentration of the water droplets or small ice crystals is compromised in the absence of a FSSP probe.

5. Conclusions

[46] In this paper, the results of a case study (21 May 2004) during the ASTAR airborne campaign in the southeast of the Svalbard Archipelago were presented. A detailed in situ characterization of the microphysical and optical properties of an Arctic mixed-phase nimbostratus cloud has been performed. The CPI observations showed that each cloud layer had distinctive but relatively homogeneous ice crystal morphology. Although the majority of the ice particles were classified as irregularly shaped particles, a high occurrence of columns and needles was found in layers characterized by temperatures ranging from −3°C to −6°C. Stellars and plates were observed at temperatures lower than −8°C. An interesting feature was the presence of large supercooled water droplets with diameters close to 500 μm when the temperature of the cloud layers was higher than −2°C. Therefore, the wide variety of ice crystal shapes and liquid water fractions experienced in the cloud system was an ideal case to study the influence of ice crystal habit on optical properties in mixed-phase conditions.

[47] In this respect, a principal component analysis (PCA) of the phase functions measured by the polar nephelometer (PN) was conducted. The results showed that the information content of the PN scattering measurements at a wavelength of 0.8 μm was sufficient to detect changes in cloud particle shape and liquid water fraction. Indeed, the optical patterns revealed by the PCA were consistent with the particle shape classification derived from the CPI measurements. One conclusion is that the synergy between the CPI and PN instruments can be exploited to link the microphysical and shape properties of cloud particles to their single-scattering properties. However, this is only true for particles with sizes larger than 50 μm as the optical contribution of small particles could not be directly determined. To study the issue of the influence of small particles (with sizes lower than 50 μm) on the optical properties, an iterative inversion algorithm using light-scattering modeling was applied to the PN phase functions measurements. The inversion results showed that small ice crystals contribute to at least 50% of the scattering coefficient of the cloud layers dominated by the ice phase. Additionally, the retrievals confirmed that idealized geometric shape models representing ensembles of deeply rough ice crystals combined with a population of water droplets were able to describe the scattering properties of the mixed-phase cloud. The optical properties of the cloud layers dominated by the liquid water phase (i.e., with an asymmetry factor greater than 0.83) can be modeled by a mixture of water droplets (representing at least 90% of the total scattering coefficient) and small droxtal shaped ice crystals. Cloud layers characterized by an asymmetry parameter around 0.81 were essentially composed of irregular shaped ice crystals and water droplets. Their scattering properties can be reproduced by a combination of water droplets (75%) and a mixture of rough columns and aggregates (25%). When the ice phase prevailed ($g < 0.80$), the optical properties of the cloud layers were modeled either by a mixture of droplets (35%) and rough plates (65%) or a combination of droplets (15%) and rough columns (85%) with a varying aspect ratio. However, the maximum variability of the retrieved concentration, effective size, and TWC caused by changes in the microphysical model can reach 140%, 80%, and 75%, respectively, for ice dominated cloud layers. It was also shown that the retrieved bulk microphysical parameters can substantially differ from the measurements (by several times for the effective size and up to 3 orders of magnitude for the number concentration). With the instrument payload onboard the aircraft, it was not possible to evaluate accurately possible effects of shattering artifacts on the measurements. This strengthens the fact that new particle imaging probes with high pixel resolution (2D-S or CIP for example) should be used to quantify the contribution of shattering to optical properties. Finally, it should be noted that these results hold only for this specific case study and this methodology should be applied to larger data sets of Arctic mixed-phase cloud properties.

[48] **Acknowledgments.** This work was funded by the Institut Polaire Français Paul Emile Victor (IPEV) and by a grant from the CNRS/INSU. We thank the members of OPTIMARE GmbH and DLR (Deutsches Zentrum für Luft- und Raumfahrt) who organized the experiment management and aircraft operations during the ASTAR 2004 campaign. We acknowledge C. Gourbeyre and J.-F. Fournol (LaMP) for their technical assistance. The authors thank the two anonymous reviewers for their help in improving the manuscript. This research was supported by the Centre National d'Etudes Spatiales (CNES) and the Institut National des Sciences de l'Univers (INSU/PNTS).

References

Arctic Climate Impact Assessment (2004), *Impacts of a Warming Arctic*, 139 pp., Cambridge Univ. Press, New York.

Baran, A. J. (2009), A review of the light scattering properties of cirrus, *J. Quant. Spectrosc. Radiat. Transfer*, *110*, 1239–1260, doi:10.1016/j.jqsrt.2009.02.026.

Baran, A. J., and P. N. Francis (2004), On the radiative properties of cirrus cloud at solar and thermal wavelengths: A test of model consistency using high-resolution airborne radiance measurements, *Q. J. R. Meteorol. Soc.*, *130*(598), 763–778, doi:10.1256/qj.03.151.

Baum, B. A., P. Yang, Y.-X. Hu, and Q. Feng (2010), The impact of ice particle roughness on the scattering phase matrix, *J. Quant. Spectrosc. Radiat. Transfer*, *111*, doi:10.1016/j.jqsrt.2010.07.008.

Cox, C., and W. Munk (1954), Measurement of the roughness of the sea surface from photographs of the Sun's glitter, *J. Opt. Soc. Am.*, *44*, 838–850, doi:10.1364/JOSA.44.000838.

Doutriaux-Boucher, M., J. C. Buriez, G. Brogniez, L. C. Labonnote, and A. J. Baran (2000), Sensitivity of retrieved POLDER directional cloud optical thickness to various ice particle models, *Geophys. Res. Lett.*, *27*(1), 109–112, doi:10.1029/1999GL010870.

Ehrlich, A., E. Bierwirth, M. Wendish, J.-F. Gayet, G. Mioche, A. Lampert, and J. Heintzenberg (2008), Cloud phase identification of low-level Arctic clouds from airborne spectral radiation measurements: Test of three approaches, *Atmos. Chem. Phys.*, *8*, 7493–7505, doi:10.5194/acp-8-7493-2008.

Engvall, A.-C., R. Krejci, J. Ström, R. Treffeisen, R. Scheele, O. Hermansen, and J. Paatero (2008), Changes in aerosol properties during spring-summer period in the Arctic troposphere, *Atmos. Chem. Phys.*, *8*, 445–462, doi:10.5194/acp-8-445-2008.

Francis, P. N., J. S. Foot, and A. J. Baran (1999), Aircraft measurements of the solar and infrared radiative properties of cirrus and their dependence on ice crystal shape, *J. Geophys. Res.*, *104*(D24), 31,685–31,695, doi:10.1029/1999JD900438.

Garrett, T. J., P. V. Hobbs, and H. Gerber (2001), Shortwave, single-scattering properties of arctic ice clouds, *J. Geophys. Res.*, *106*(D14), 15,155–15,172, doi:10.1029/2000JD900195.

Gayet, J.-F., O. Crépel, J.-F. Fournol, and S. Oshchepkov (1997), A new airborne polar nephelometer for the measurements of optical and microphysical cloud properties: 1. Theoretical design, *Ann. Geophys.*, *15*, 451–459, doi:10.1007/s00585-997-0451-1.

Gayet, J.-F., S. Asano, A. Yamazaki, A. Uchiyama, A. Sinyuk, O. Jourdan, and F. Auriol (2002a), Two case studies of winter continental-type water and mixed-phase stratocumuli over the sea 1.Microphysical and optical properties, *J. Geophys. Res.*, *107*(D21), 4569, doi:10.1029/2001JD001106.

Gayet, J.-F., F. Auriol, A. Minikin, J. Ström, M. Seifert, R. Krejci, A. Petzold, G. Febvre, and U. Schumann (2002b), Quantitative measurement of the microphysical and optical properties of cirrus clouds with four different in situ probes: Evidence of small ice crystals, *Geophys. Res. Lett.*, *29*(24), 2230, doi:10.1029/2001GL014342.

Gayet, J.-F., V. Shcherbakov, H. Mannstein, A. Minikin, U. Schumann, J. Ström, A. Petzold, J. Ovarlez, and F. Immler (2006), Microphysical and optical properties of midlatitudes cirrus clouds observed in the southern hemisphere during INCA, *Q. J. R. Meteorol. Soc.*, *132*(621), 2719–2748, doi:10.1256/qj.05.162.

Gayet, J.-F., R. Treffeisen, A. Helbig, J. Bareiss, A. Matsuki, A. Herber, and A. Schwarzenboeck (2009a), On the onset of the ice phase in boundary-layer Arctic clouds, *J. Geophys. Res.*, *114*, D19201, doi:10.1029/2008JD011348.

Gayet, J.-F., G. Mioche, A. Dörnbrack, A. Ehrlich, A. Lampert, and M. Wendisch (2009b), Microphysical and optical properties of Arctic mixed-phase clouds: The 9 April 2007 case study, *Atmos. Chem. Phys.*, *9*, 6581–6595, doi:10.5194/acp-9-6581-2009.

Gerber, H., Y. Takano, T. J. Garrett, and P. V. Hobbs (2000), Nephelometer measurements of the asymmetry parameter, volume extinction coefficient and backscatter ratio in Arctic clouds, *J. Atmos. Sci.*, *57*, 3021–3034, doi:10.1175/1520-0469(2000)057<3021:NMOTAP>2.0.CO;2.

Heymsfield, A. J. (2007), On measurements of small ice particles in clouds, *Geophys. Res. Lett.*, *34*, L23812, doi:10.1029/2007GL030951.

Intergovernmental Panel on Climate Change (IPCC) (2001), *Climate Change: The Scientific Basis*, edited by J. T. Houghton et al., 944 pp., Cambridge Univ. Press, New York.

Intergovernmental Panel on Climate Change (IPCC) (2007), *Climate Change 2007: The Fourth Assessment Report of the IPCC*, Cambridge Univ. Press, New York.

Jourdan, O., S. Oshchepkov, J.-F. Gayet, V. Shcherbakov, and H. Isaka (2003a), Statistical analysis of cloud light scattering and microphysical properties obtained from airborne measurements, *J. Geophys. Res.*, *108* (D5), 4155, doi:10.1029/2002JD002723.

Jourdan, O., S. Oshchepkov, V. Shcherbakov, J.-F. Gayet, and H. Isaka (2003b), Assessment of cloud optical parameters in the solar region: Retrievals from airborne measurements of scattering phase functions, *J. Geophys. Res.*, *108*(D18), 4572, doi:10.1029/2003JD003493.

Korolev, A., and G. A. Isaac (2005), Shattering during sampling by OAPs and HVPS. Part I: Snow particles, *J. Atmos. Oceanic Technol.*, *22*, 528–543, doi:10.1175/JTECH1720.1.

Korolev, A. V., J. W. Strapp, G. A. Isaac, and A. N. Nevzorov (1998), The Nevzorov airborne hot-wire LWC-TWC probe: Principle of operation and performance characteristics, *J. Atmos. Oceanic Technol.*, *15*, 1495–1510, doi:10.1175/1520-0426(1998)015<1495:TNAHWL>2.0.CO;2.

Korolev, A. V., G. A. Isaac, J. W. Strapp, and A. N. Nevzorov (1999), In situ measurements of effective diameter and effective droplet number concentration, *J. Geophys. Res.*, *104*(D4), 3993–4003, doi:10.1029/1998JD200071.

Korolev, A. V., G. A. Isaac, S. G. Cober, J. W. Strapp, and J. Hallett (2003), Microphysical characterization of mixed-phase clouds, *Q. J. R. Meteorol. Soc.*, *129*(587), 39–65, doi:10.1256/qj.01.204.

Korolev, A. V., J. W. Strapp, G. A. Isaac, and E. Emery (2008), Improved airborne hot-wire measurements of ice water content in clouds, paper presented at International Conference on Clouds and Precipitation, Int. Comm. on Clouds and Precip., Cancun, Mexico.

Labonnote, L. C., G. Brogniez, M. Doutriaux-Boucher, J. Buriez, J.-F. Gayet, and H. Chepfer (2000), Modeling of light scattering in cirrus clouds with inhomogeneous hexagonal monocrystals: Comparison with in situ and ADEOS-POLDER measurements, *Geophys. Res. Lett.*, *27*(1), 113–116, doi:10.1029/1999GL010839.

Lawson, R. P., B. A. Baker, C. G. Schmitt, and T. L. Jensen (2001), An overview of microphysical properties of Arctic clouds observed in May and July 1998 during FIRE ACE, *J. Geophys. Res.*, *106*(D14), 14,989–15,014, doi:10.1029/2000JD900789.

Lawson, R. P., D. O'Connor, P. Zmarzly, K. Weaver, B. Baker, and Q. Mo (2006), The 2D-S (stereo) probe: Design and preliminary tests of a new airborne high-speed, high-resolution particle imaging probe, *J. Atmos. Oceanic Technol.*, *23*, 1462–1477, doi:10.1175/JTECH1927.1.

McFarquhar, G. M., G. Zhang, M. R. Poellot, G. L. Kok, R. McCoy, T. Tooman, A. Fridling, and A. J. Heymsfield (2007), Ice properties of single-layer stratocumulus during the Mixed-Phase Arctic Cloud Experiment: 1. Observations, *J. Geophys. Res.*, *112*, D24201, doi:10.1029/2007JD008633.

Oshchepkov, S., H. Isaka, J.-F. Gayet, A. Sinyuk, F. Auriol, and S. Havemann (2000), Microphysical properties of mixed-phase & ice clouds retrieved from in situ airborne "polar nephelometer" measurements, *Geophys. Res. Lett.*, *27*(2), 209–212, doi:10.1029/1999GL010784.

Saunders, C., J. Rimmer, P. Jonas, J. Arathoon, and C. Liu (1998), Preliminary laboratory studies of the optical scattering properties of the crystal clouds, *Ann. Geophys.*, *16*, 618–627, doi:10.1007/s00585-998-0618-4.

Schwarzenboeck, A., G. Mioche, A. Armetta, A. Herber, and J.-F. Gayet (2009), Response of the Nevzorov hot wire probe in clouds dominated by droplet conditions in the drizzle size range, *Atmos. Meas. Tech.*, *2*(2), 779–788, doi:10.5194/amt-2-779-2009.

Shcherbakov, V., J.-F. Gayet, B. Baker, and P. Lawson (2006), Light scattering by single natural ice crystals, *J. Atmos. Sci.*, *63*, 1513–1525, doi:10.1175/JAS3690.1.

Shcherbakov, V., J.-F. Gayet, G. Febvre, A. J. Heymsfield, and G. Mioche (2010), Probabilistic model of shattering effect on in-cloud measurements, *Atmos. Chem. Phys. Discuss.*, *10*, 11,009–11,046, doi:10.5194/acpd-10-11009-2010.

Stachlewska, I. S., G. Wehrle, B. Stein, and R. Neuber (2004), Airborne mobile aerosol lidar for measurements of Arctic aerosol, in *Proceeding of the 22nd International Laser Radar Conference*, edited by G. Pappalardo and A. Amodeo, pp. 87–89, ESA, Paris.

Stephens, G. L., et al. (2002), The CloudSat mission and the A-train: A new dimension of space-based observations of clouds and precipitation, *Bull. Am. Meteorol. Soc.*, *83*, 1771–1790, doi:10.1175/BAMS-83-12-1771.

Vavrus, S. (2004), The impact of cloud feedbacks on arctic climate under greenhouse forcing, *J. Clim.*, *17*, 603–615, doi:10.1175/1520-0442(2004)017<0603:TIOCFO>2.0.CO;2.

Verlinde, J., et al. (2007), The mixed-phase Arctic cloud experiment (M-PACE), *Bull. Am. Meteorol. Soc.*, *88*, 205–221, doi:10.1175/BAMS-88-2-205.

Winker, D., and C. Trepte (2007), Distribution and Characteristics of polar clouds from CALIOP, paper presented at A-Train-Lille 07 Symposium, CNES, Lille, France.

Xie, Y., P. Yang, B.-C. Gao, G. W. Kattawar, and M. I. Mishchenko (2006), Effect of ice crystal shape and effective size on snow bidirectional reflectance, *J. Quant. Spectrosc. Radiat. Transfer*, *100*, 457–469, doi:10.1016/j.jqsrt.2005.11.056.

Xie, Y., P. Yang, G. W. Kattawar, P. Minnis, and Y. X. Hu (2009), Effect of the inhomogeneity of ice crystals on retrieving ice cloud optical thickness and effective particle size, *J. Geophys. Res.*, *114*, D11203, doi:10.1029/2008JD011216.

Yang, P., and K. N. Liou (1996), Geometric-optics-integral-equation method for light scattering by nonspherical ice crystals, *Appl. Opt.*, *35*, 6568–6584, doi:10.1364/AO.35.006568.

Yang, P., and K. N. Liou (1998), Single-scattering properties of complex ice crystals in terrestrial atmosphere, *Contrib. Atmos. Phys.*, *71*, 223–248.

Yang, P., K. N. Liou, K. Wyser, and D. Mitchell (2000), Parameterization of the scattering and absorption properties of individual ice crystals, *J. Geophys. Res.*, *105*(D4), 4699–4718, doi:10.1029/1999JD900755.

Yang, P., B. A. Baum, A. J. Heymsfield, Y. X. Hu, H.-L. Huang, S.-C. Tsay, and S. Ackerman (2003), Single-scattering properties of droxtals, *J. Quant. Spectrosc. Radiat. Transfer*, *79–80*, 1159–1169, doi:10.1016/S0022-4073(02)00347-3.

Yang, P., G. W. Kattawar, G. Hong, P. Minnis, and Y. Hu (2008a), Uncertainties associated with the surface texture of ice particles in satellite-based retrieval of cirrus clouds: Part I. Single-scattering properties of ice crystals with surface roughness, *IEEE Trans. Geosci. Remote Sens.*, *46*, 1940–1947, doi:10.1109/TGRS.2008.916471.

Yang, P., G. Hong, G. W. Kattawar, P. Minnis, and Y. Hu (2008b), Uncertainties associated with the surface texture of ice particles in satellite-based retrieval of cirrus clouds: Part II. Effect of particle surface roughness on retrieved cloud optical thickness and effective particle size, *IEEE Trans. Geosci. Remote Sens.*, *46*, 1948–1957, doi:10.1109/TGRS.2008.916472.

Zhang, Z., P. Yang, G. W. Kattawar, S.-C. Tsay, B. A. Baum, Y. Hu, A. J. Heymsfield, and J. Reichardt (2004), Geometrical-optics solution to light scattering by droxtal ice crystals, *Appl. Opt.*, *43*, 2490–2499, doi:10.1364/AO.43.002490.

T. J. Garrett, Department of Atmospheric Sciences, University of Utah, Salt Lake City, UT 84103, USA.

J.-F. Gayet, O. Jourdan, G. Mioche, A. Schwarzenböck, V. Shcherbakov, and J. Vidot, Laboratoire de Météorologie Physique, Université Blaise Pascal, OPGC/CNRS UMR 6016, F-63177 Clermont-Ferrand, France. (o.jourdan@opgc.univ-bpclermont.fr)

Y. Xie and P. Yang, Department of Atmospheric Sciences, Texas A&M University, College Station, TX 77843, USA.